

CRYSTALLINE SILICATE EMISSION IN THE PROTOSTELLAR BINARY SERPENS-SVS20

DAVID R. CIARDI

Michelson Science Center/Caltech
 770 South Wilson Avenue, M/S 100-22
 Pasadena, CA 91125

CHARLES M. TELESKO, CHRISTOPHER PACKHAM,
 CYNTHIA GÓMEZMARTIN, JAMES T. RADOMSKI
 University of Florida, Department of Astronomy
 211 Space Sciences Building, Gainesville, FL 32611

JAMES M. DE BUIZER

Gemini Observatory
 Casilla 603, La Serena, Chile

CHRIS J. PHILLIPS

Australia Telescope National Facility, CSIRO
 P.O. Box 76, Epping NSW 1710, Australia

DAVID E. HARKER

University of California, San Diego, CASS
 9500 Gilman Dr., Dept. 0424, La Jolla, CA 92093-0424
Accepted for publication in The Astrophysical Journal

ABSTRACT

We present spatially resolved mid-infrared spectroscopy of the class I/flat-spectrum protostellar binary system SVS20 in the Serpens cloud core. The spectra were obtained with the mid-infrared instrument T-ReCS on Gemini-South. SVS20-South, the more luminous of the two sources, exhibits a mid-infrared emission spectrum peaking near 11.3 μm , while SVS20-North exhibits a shallow amorphous silicate absorption spectrum with a peak optical depth of $\tau \sim 0.3$. After removal of the line-of-sight extinction by the molecular common envelope, the “protostar-only” spectra are found to be dominated by strong amorphous olivine emission peaking near 10 μm . We also find evidence for emission from crystalline forsterite and enstatite associated with both SVS20-S and SVS20-N. The presence of crystalline silicate in such a young binary system indicates that the grain processing found in more evolved HAeBe and T Tauri pre-main sequence stars likely begins at a relatively young evolutionary stage, while mass accretion is still ongoing.

Subject headings: infrared: ISM — infrared: stars — ISM: individual (Serpens, SVS20, SMM6) stars: formation — stars: pre-main-sequence

1. INTRODUCTION

Silicates found in the general interstellar medium are amorphous dust grains, while in T Tauri and HAeBe pre-main sequence stars (e.g., Meeus et al. 2003; Przygodda et al. 2003; van Boekel et al. 2003; Kessler-Silacci et al. 2005), in debris disks surrounding main sequence stars (e.g., β Pic & HD 145263; Telesco & Knacke 1991; Knacke et al. 1993; Honda et al. 2004), and in our own solar system (e.g., Comet C/1996 Q1; Harker et al. 1999), we observe both amorphous and crystalline silicate grains. This distinction between the dust in the ISM and dust in stellar disks implies a transformation of the dust during the early phases of stellar and disk evolution when planets form. Thus, it is reasonable that probing the evolution of the silicate grains may provide insight into the concurrent planetary evolution.

The data illuminating the evolution of the dust are

still sparse and, at times, contradictory. For example, some young stellar objects contain larger amorphous silicate grains indicative of grain growth, while other young stellar objects of similar evolutionary status have signs of crystalline silicate grains, with no simple picture indicating at what stage in the evolutionary sequence significant grain growth and crystallization take place (e.g., Meeus et al. 2003; Przygodda et al. 2003; van Boekel et al. 2003). While a general evolutionary sequence of dust processing seems to be emerging (e.g., Kessler-Silacci et al. 2005), other significant issues, such as the possible dependence of the grain evolution on the source luminosity and temperature, and the effect of nearby companions in multiple star systems, are not yet understood.

As part of our binary protostellar program (see also Ciardi et al. 2003), we observed the mid-infrared emission of the protostellar binary SVS20 (Strom, Vrba, & Strom 1976). SVS20 is a member of

the young protostellar cluster (age $\sim 10^5$ yr; Kass et al. 2004) located in the Serpens cloud core ($d \simeq 250$ pc, Straizys, Černis, & Bartašiūtė 1996). SVS20 is a sub-mm source (SMM6; Casali, Eiroa, & Duncan 1993) and was first identified as a binary system by Eiroa et al. (1987). The components (SVS20-South and SVS20-North) are separated by $1''.5$ (~ 375 AU) at a position angle of $9^\circ 9'$. The two sources have similar infrared spectral energy distributions with spectral indices appropriate for class I/flat spectrum protostars (Haisch et al. 2002). From the $3.1 \mu\text{m}$ ice absorption feature, Eiroa & Leinert (1987) determined that the binary components share a common envelope with an extinction of $A_V \approx 14$ mag. In addition, near-infrared polarization observations are centro-symmetric about SVS20 indicating that SVS20 has partially evacuated the cavity immediately surrounding the binary system, potentially offering a more direct view of the central protostars (Huard, Weintraub, & Kastner 1997).

ISOCAM CVF observations of SVS20, with an angular resolution of $6'' \text{ pixel}^{-1}$, indicated amorphous silicate in both absorption and emission (Alexander et al. 2003), but the ISO observations did not resolve SVS20-S and SVS20-N. We present spatially resolved $8 - 13 \mu\text{m}$ spectroscopy of SVS20. The spectrum of SVS20-N is dominated by amorphous silicate absorption, while the spectrum of SVS20-S exhibits strong crystalline silicate emission. The clear differences in the spectra indicate differing levels of dust processing for the two components of the binary system.

2. OBSERVATIONS AND DATA REDUCTION

2.1. Spectroscopy

Mid-infrared ($8 - 13 \mu\text{m}$) spectroscopic observations of SVS20 were made on 2003 October 05 (UT) using the Thermal Region Camera and Spectrograph (T-ReCS; Telesco et al. 1998) on the Gemini South 8 m telescope. T-ReCS utilizes a 320×240 pixel Si:As blocked impurity band detector, with a spatial scale of $0''.089 \text{ pixel}^{-1}$ and a field of view of $28''.8 \times 21''.6$. The observations utilized the low-resolution grating ($R \sim 111$ at $\lambda_c = 10.5 \mu\text{m}$) and a $0''.72$ slit. The N-band filter ($\lambda_o = 10.36 \mu\text{m}$, $\Delta\lambda = 5.2 \mu\text{m}$) served as the blocking filter. The spectral dispersion (along the 320 pixel-axis) is $0.022045 \mu\text{m pix}^{-1}$. T-ReCS was rotated so that both components were positioned in the slit simultaneously. We used a standard $15''$ north-south chop-nod sequence, with an on-source integration time of 150 s. Standard NOAO IRAF packages were used to reduce the data and extract the spectra. HD 187642 (A_7V , $F_\nu[9.8 \mu\text{m}] = 33 \pm 1 \text{ Jy}^1$) was observed for telluric line removal and flux calibration. The zero point of the wavelength scale was set using the deepest point of the telluric ozone feature at $9.495 \mu\text{m}$. The signal-to-noise of the spectra is $S/N \approx 50 - 70$, where the noise has been estimated from the pixel-to-pixel variations in the spectra.

2.2. Photometry

Supplemental photometry was acquired on SVS20 with T-ReCS as part of the setup for the spectroscopic observations. T-ReCS imaging was performed in the $11.7 \mu\text{m}$

narrow-band ($\Delta\lambda = 1.1 \mu\text{m}$) filter, with an integration time of 60 sec. Figure 1 displays the T-ReCS $11.7 \mu\text{m}$ image. At the spatial resolution of T-ReCS, the binary system is clearly resolved with no detection of extended emission connecting the system components; all of the mid-infrared emission from SVS20-S and SVS20-N emanates from within ~ 100 AU of the central protostars. Flux calibration was obtained from $11.7 \mu\text{m}$ imaging of HD 187642. Standard NOAO IRAF packages were used to reduce the data and extract the aperture photometry.

SVS20 was also imaged on 2002 July 21 (UT) with the Thermal Infrared Multimode Instrument-2 (TIMMI2) on the ESO La Silla 3.6m telescope. TIMMI2 has a 320×240 pixel Si:As blocked impurity band detector, with a pixel scale of $0''.2 \text{ pixel}^{-1}$. SVS20 was imaged in three narrow-band filters ($N\lambda 10.4$, $\Delta\lambda = 1 \mu\text{m}$; $N\lambda 11.9$, $\Delta\lambda = 1.2 \mu\text{m}$; $N\lambda 12.9$, $\Delta\lambda = 1.2 \mu\text{m}$). A standard north-south chop-nod sequence with a $10''$ on-chip chop throw was used. The integration time was 258 s. The data were reduced with custom-written IDL routines for the TIMMI2 data format. Standard aperture photometry was performed using an IDL version of DAOPHOT. Flux calibration was obtained from observations of HD 187642².

The T-ReCS spectra, along with the corresponding photometry from T-ReCS, TIMMI2, and the literature, are summarized in Figure 2 and Table 1. In Figure 2, the continuum levels for the mid-infrared emission underlying the observed silicate features are estimated via a linear interpolation of the mean flux density levels near the endpoints of the spectra: $[8.0 - 8.1 \mu\text{m}]$ & $[12.8 - 12.9 \mu\text{m}]$. The T-ReCS spectroscopic flux densities are in good agreement with the T-ReCS and TIMMI2 photometry and with the unresolved IRAS and ISO (not shown, see Alexander et al. 2003) observations. The $10.78 \mu\text{m}$ flux densities for SVS20 reported by Haisch et al. (2002) are systematically lower by $\sim 25\%$. Given the general agreement between the ISO, IRAS, T-ReCS, and TIMMI2 data, the 1998 flux densities reported by Haisch et al. (2002) may be discrepant or may represent true intrinsic mid-infrared variability of SVS20 (e.g., Liu et al. 1996).

3. DISCUSSION

The primary result of this paper is the visibly different mid-infrared spectra exhibited by the two components of the binary system (Fig. 2). Relative to the continuum levels, SVS20-S displays a strong silicate emission spectrum, while SVS20-N exhibits a shallow silicate absorption spectrum. Alexander et al. (2003) modeled the *unresolved* ISOCAM CVF observations of SVS20 as a combination of amorphous silicate absorption ($\tau \approx 0.6 - 0.8$; $A_V \sim 10 - 14$ mag) superposed upon amorphous silicate emission ($\tau \approx -0.4$). The T-ReCS spectra show that SVS20-S is responsible for the majority of the observed silicate emission in SVS20.

3.1. Component Luminosities

Superficially, SVS20-S and SVS20-N have similar looking infrared spectral energy distributions (SED) with $2.2 - 10 \mu\text{m}$ spectral indices $[\alpha = -d \log(\nu F_\nu)/d \log(\nu)]$ of $\alpha_{\text{South}} = 0.11 \pm 0.01$, $\alpha_{\text{North}} = 0.38 \pm 0.03$. These spectral indices are redder than those calculated by

¹ http://www.gemini.edu/sciops/instruments/miri/filters/stdfluxes_zero.txt ² <http://www.ls.eso.org/lasilla/sciops/3p6/timmi/html/stand.html>

Haisch et al. (2002), but still indicate that both components are class I/flat spectrum protostars.

To explore the SEDs more carefully and parameterize the relative temperatures and luminosities of the central protostars, we have fitted the near-infrared (0.9 – 3.5 μm) photometry from the literature with a blackbody function modified by a line-of-sight extinction curve: $S_\nu = \Omega B_\nu(T_d) \exp(-A_\nu/1.086)$, where $B_\nu(T)$ is the Planck function, A_ν is the frequency-dependent extinction ($R=3.1$ assumed, Mathis 1990), and Ω is the solid angle.

A temperature range of $T = 500 - 50000$ K in steps of 100 K and an extinction range of $A_V = 0 - 50$ mag in steps of 0.05 mag were tested. Uncertainties for the blackbody fitting were estimated via a Monte Carlo simulation where the data points were randomly adjusted by their individual uncertainties, and the data were re-fitted; the model parameter uncertainties were estimated from the standard deviations of the best fits.

Of course, the SEDs arise from multiple emission sources of various temperatures within the young stellar objects (e.g., central protostar, accretion emission), but the near-infrared emission ($\lambda \lesssim 3 \mu\text{m}$) should be primarily from the stellar photospheres (e.g., Greene & Lada 1997), allowing us to estimate the relative temperatures and luminosities of the central objects within each component. Results of the fitting are shown in Figure 3. The SED for SVS20-N is reasonably well fit with a $T_{\text{eff}} = 3300 \pm 500$ K blackbody screened by an extinction of $A_V = 26.5 \pm 1.5$ mag ($\chi_\nu^2 \approx 2$) with a luminosity of $L_* \approx 0.9 L_\odot$ – similar to the values for other low-mass young stellar objects (e.g., IRAS 04016+2610: $T_{\text{eff}} = 3300 - 4200$, $A_V = 19 - 21$, Ishii, Tamura, & Itoh 2004).

The SED modeling for SVS20-S is less constrained. The reduced chi-square for the fits are never better than $\chi_\nu^2 \approx 5$, regardless of the combination of temperature and extinction. There is a broad localized minimum for the temperature range $T_{\text{eff}} \approx 7000 - 10000$ K with corresponding extinctions of $A_V = 28 - 29$ mag. Models with lower extinction have local minima at correspondingly lower temperatures, but the fits are significantly worse ($\chi_\nu^2 > 6$). Models with higher extinction do not have localized minima; the reduced chi-squares asymptotically approach $\chi_\nu^2 \sim 5$. Figure 4 displays the dependence of the model chi-square as a function of temperature for four different extinction levels. We conservatively estimate that the central protostar for SVS20-S is a 10,000 K blackbody, screened by ~ 30 mag of extinction – suggesting a luminosity of $L_* \approx 20 - 80 L_\odot$, which is comparable to estimates made by Eiroa & Leinert (1987).

The extinguished single-temperature blackbody fits to the near-infrared SEDs represent estimates of the total visual extinction of the central protostar by the surrounding circumstellar disk and the molecular envelope. If a common envelope contributes ~ 14 magnitudes of extinction (Eiroa & Leinert 1987), then the circumstellar material immediately surrounding each protostar extinguishes the central protostar by 10 – 15 magnitudes. The modelling reduced chi-squares of $\chi_\nu^2 \sim 2 - 5$ are likely the result of the single-temperature assumption, as evidenced by the extinguished blackbody models predicting too little 10 μm continuum emission (see Fig. 3).

3.2. The Observed Mid-Infrared Spectra

The observed mid-infrared spectrum of SVS20-S exhibits an emission feature with the peak of the emission occurring near 11.3 μm . In more evolved sources such as H AeBe stars, the emission peak at 11.3 μm is indicative of crystalline silicate (e.g., Knacke et al. 1993), as amorphous olivine particles (0.1 μm in size) emit a feature peaking near 9.7 μm (Bouwmann et al. 2001; Kessler-Silacci et al. 2005). As amorphous silicate grains grow in size, the emission feature broadens and becomes flat-topped (Bouwmann et al. 2001; Przygodda et al. 2003; van Boekel et al. 2003).

Przygodda et al. (2003) and van Boekel et al. (2003) correlate the strength of the silicate emission feature with the ratio of the 11.3 μm to the 9.8 μm flux densities. A ratio of $F_{9.8\mu\text{m}}/F_{11.3\mu\text{m}} \lesssim 1$ suggests emission from crystalline silicates (Przygodda et al. 2003). Kessler-Silacci et al. (2005) extend this technique by correlating the $F_{9.8\mu\text{m}}/F_{11.3\mu\text{m}}$ and the $F_{9.8\mu\text{m}}/F_{8.6\mu\text{m}}$ ratios. They find that the ratios are linearly correlated, and that sources with crystalline silicate emission possess lower ratios than those sources with only amorphous silicate emission.

For the observed SVS20-S spectrum, we have calculated the $F_{9.8\mu\text{m}}/F_{11.3\mu\text{m}}$ and the $F_{9.8\mu\text{m}}/F_{8.6\mu\text{m}}$ ratios from the continuum-normalized spectrum (Figure 5). We measured ratios of $F_{9.8\mu\text{m}}/F_{11.3\mu\text{m}} = 0.8 \pm 0.1$ and $F_{9.8\mu\text{m}}/F_{8.6\mu\text{m}} = 1.0 \pm 0.1$. These ratios place SVS20-S in the same region of the [8.6 μm , 9.8 μm , 11.3 μm] color-color diagram as the more evolved T Tauri star Hen 3-600A and the H AeBe star HD179218, both of which have crystalline silicate emission (see Figure 11 in Kessler-Silacci et al. 2005). However, these ratios for SVS20-S, while similar to those observed in more evolved pre-main sequence stars with known crystalline grain emission, do not take into account that SVS20-S, unlike the more evolved T Tauri and H AeBe stars, has a significant amount (~ 14 mag) of foreground absorption from the surrounding envelope (see §3.3).

For SVS20-N, the observed mid-infrared spectrum, in contrast to SVS20-S, is dominated by an absorption feature centered at 9.7 μm . The mid-infrared spectrum of SVS20-N resembles other low-mass embedded class I young stellar objects such as IRAS 04239+2436 (Kessler-Silacci et al. 2005), or IRAS 04108+2803B (Watson et al. 2004), where the amorphous silicate absorption at 9.7 μm is clearly present but shallow ($\sim 25\%$ below the continuum level). We have calculated the optical depth of the absorption based upon the estimated continuum level (Fig 2): $\tau_\nu = -\ln(\frac{F_\nu}{F_{\nu_0}})$ where F_ν is the observed flux density and F_{ν_0} is the flux density of the continuum. The optical depth for SVS20-N as a function of wavelength is presented in Figure 5. Assuming $A_V/\tau_{9.7\mu\text{m}} \approx 17$ (Rieke & Lebofsky 1985), the peak optical depth of $\tau \sim 0.3$ corresponds to a line-of-sight visual extinction of only $A_V \sim 5$ mag.

The extinction derived from the silicate optical depth is nearly 10 magnitudes lower than the envelope extinction implied by the 3.1 μm ice feature (Eiroa & Leinert 1987). The lower observed optical depth implies that the mid-infrared spectrum of SVS20-N contains silicate emission that is filling in partially ($\sim 75\%$) the line-of-sight absorption from the surrounding envelope. In addition,

there is a decrease in the optical depth near $11.3 \mu\text{m}$ indicating that some of the emission may be from crystalline silicate emission. In the following section, the effect of the envelope absorption on the innate mid-infrared emission from SVS20-S and SVS20-N is discussed.

3.3. Correction for the Envelope Extinction

To probe the effects of the line-of-sight absorption by the surrounding common molecular envelope on the observed mid-infrared spectra, we developed a model of the expected extinction by the dust grains contained within the common envelope. Indices of refraction of amorphous olivine (Dorschner et al. 1995) were used with Mie theory to calculate the wavelength-dependent extinction coefficients for particles $0.15 \mu\text{m}$ in diameter. Based upon the $3.1 \mu\text{m}$ ice feature (Eiroa & Leinert 1987), we assumed that the peak line-of-sight extinction produced by the envelope is $A_V = 14 \text{ mag}$ for both SVS20-S and SVS20-N. The envelope dust was assumed to be cool ($\sim 15 \text{ K}$) enough to produce no substantial mid-infrared emission of its own (Testi & Sargent 1998). The mid-infrared spectra corrected for the envelope extinction [$F_{\nu o} = F_{\nu} \exp(\tau_{env})$] are presented in Figure 6. These spectra represent the expected mid-infrared emission of the protostars, after the removal of the surrounding common envelope extinction.

The protostellar mid-infrared emission is dominated by the emission of amorphous silicates, which, in both protostars, peaks at $\lambda \approx 10 \mu\text{m}$. The silicate emission above the continuum from SVS20-S is four times the strength of the silicate emission from SVS20-N. This is likely a direct result of the different temperatures and luminosities of the central objects (§3.1), where SVS20-S is three times hotter and 20 times more luminous than SVS20-N. After the extinction correction, the $2.2 - 10 \mu\text{m}$ spectral indices for SVS20-S and SVS20-N, respectively, are $\alpha \approx -0.3$ and $\alpha \approx -0.1$, suggesting that while the binary is still deeply embedded, the components of SVS20 may be evolving towards Class II young stellar objects.

If we apply the flux density ratios developed by Przygodda et al. (2003), van Boekel et al. (2003), and Kessler-Silacci et al. (2005), we find for SVS20-S, that $F_{9.8\mu\text{m}}/F_{11.3\mu\text{m}} \approx 1.3$ and $F_{9.8\mu\text{m}}/F_{8.6\mu\text{m}} \approx 2.0$, and for SVS20-N, that $F_{9.8\mu\text{m}}/F_{11.3\mu\text{m}} \approx 1.3$ and $F_{9.8\mu\text{m}}/F_{8.6\mu\text{m}} \approx 1.5$. These new ratios are significantly larger than those derived prior to the correction of the line-of-sight extinction, and taken by themselves place SVS20-S and SVS20-N among T Tauri and HAeBe stars with no detectable crystalline emission. However, while the spectra for both SVS20-S and SVS20-N are dominated by amorphous olivine emission, it is evident from Fig. 6 that there is also additional emission near $11.3 \mu\text{m}$ producing a shoulder on the broader olivine emission feature. To study this feature in more detail, we have fitted a local continuum to the spectra between $10.5 \leq \lambda \leq 12.1 \mu\text{m}$. The continuum levels for the mid-infrared emission underlying the observed features are estimated via a quadratic interpolation of the flux density levels near the endpoints: $[10.5 - 10.7 \mu\text{m}]$ & $[11.8 - 12.1 \mu\text{m}]$. The continuum-subtracted spectra are displayed in the bottom panel of Figure 6.

The emission in this local region from SVS20-S remains four times the strength of the emission from SVS20-

N, but both sources show clear peaks near $\lambda \approx 11.3 \mu\text{m}$ and $\lambda \approx 10.9 \mu\text{m}$. The peak centered near $11.3 \mu\text{m}$ tentatively is associated with forsterite Mg_2SiO_4 (Bouwman et al. 2001). This forsterite peak is always accompanied by an additional narrow peak at $10 \mu\text{m}$ which is evident in both sources (top, Fig. 6). The narrower peak at $\lambda \approx 10.9 \mu\text{m}$ tentatively is associated with enstatite MgSiO_3 (Bouwman et al. 2001). Enstatite is also associated with broader peaks near $8.5 - 9.5 \mu\text{m}$ and $10.5 \mu\text{m}$. Evidence for emission from these features in excess of the amorphous silicate emission can also be seen in both sources (top, Fig. 6). Finally, as mentioned in §2, there is no resolved extended mid-infrared emission indicating that all of the silicate emission (amorphous and crystalline) is contained within $\sim 100 \text{ AU}$ of the central protostars. Thus, both SVS20-S and SVS20-N appear to have begun processing and annealing the dust grains within their local environments.

4. SUMMARY

We have presented spatially resolved mid-infrared ($8 - 13 \mu\text{m}$) spectra of the class I/flat-spectrum protostellar binary Serpens SVS20-(S,N). We summarize our results as follows:

(1) Although SVS20-S and SVS20-N have similar broadband spectral energy distributions, our simple models suggest that the temperatures and luminosities of the two central objects are quite different. The central protostellar source in SVS20-S has an effective temperature of $T_{eff} \approx 7000 - 10000 \text{ K}$ and a luminosity of $L_{\star} \approx 20 - 80 L_{\odot}$, while the central protostar in SVS20-N has an effective temperature of $T_{eff} \sim 3300 \text{ K}$ and a luminosity of only $L_{\star} \sim 0.9 L_{\odot}$.

(2) The observed mid-infrared spectra of the binary components also differ. The spectrum of SVS20-S exhibits strong silicate emission, while that of SVS20-N is dominated by shallow amorphous silicate absorption. After correction for the line-of-sight common envelope extinction, the mid-infrared emission of the protostars for the two objects are dominated by amorphous silicate emission, although the emission feature from SVS20-S is four times the strength of the emission feature from SVS20-N. In addition to the amorphous silicate emission, both SVS20-S and SVS20-N show evidence for the presence of emission from crystalline silicate in the form of forsterite and enstatite.

(3) The different luminosities of the two components may be responsible for the different amounts of crystalline silicate emission observed in each component. The lower luminosity of SVS20-N may have resulted in longer processing times for the circumstellar material, although the apparent presence of crystalline emission indicates that, even for lower mass young stellar objects, crystallization occurs relatively early in the star formation process.

In order to understand more fully the binary system SVS20, modelling of the complete spectral energy distribution coupled with accretion processes and mineralogy will be the subject of a future paper. The differences in the spectra clearly indicate a different level of dust processing between the two protostars. The presence of crystalline silicates in such a young binary protostellar system indicates that the grain growth and processing found in more evolved pre-main sequence stars, in debris

disks around main sequence stars, and in comets in our own solar system begins at a much younger evolutionary stage while accretion is still ongoing.

The authors would like to thank the engineering staff at the University of Florida and the staff at Gemini Observatories for their help and outstanding support in making T-ReCS a success. The authors thank the referee whose comments improved the paper greatly. The research was supported in part by NSF grant AST-0098392 to C.M. and by NSF grant AST-0206617 to C.P. and

J.T.R. Based on observations obtained at the Gemini Observatory, which is operated by the Association of Universities for Research in Astronomy, Inc., under a cooperative agreement with the NSF on behalf of the Gemini partnership: the National Science Foundation (United States), the Particle Physics and Astronomy Research Council (United Kingdom), the National Research Council (Canada), CONICYT (Chile), the Australian Research Council (Australia), CNPq (Brazil) and CONICET (Argentina).

REFERENCES

- Alexander, R. D., Casali, M. M., André, P., Persi, P., & Eiroa, C. 2003, *A&A*, 401, 613
- Ali, B. & Noriega-Crespo, A. 2004, *ApJ*, 613, 374
- Bouwman, J., Meeus, G., de Koter, A., Hony, S., Dominik, C., & Waters, L. B. F. M. 2001, *A&A*, 375, 950
- Casali, M. M., Eiroa, C., & Duncan, W. D. 1993, *A&A*, 275, 195
- Churchwell, E. & Koornneef, J. 1986, *ApJ*, 300, 729
- Ciardi, D. R., Telesco, C. M., Williams, J. P., Fisher, R. S., Packham, C., Piña, R., & Radomski, J. 2003, *ApJ*, 585, 392
- Dorschner, J., Begemann, B., Henning, T., Jaeger, C., & Mutschke, H. 1995, *A&A*, 300, 503
- Eiroa, C., & Leinert, Ch., 1987, *A&A*, 188, 46
- Eiroa, C., Lenzén, R., Leinert, Ch., & Hodapp, K.-W. 1987, *A&A*, 179, 171
- Greene, T. P., & Lada, C. J. 1997, *AJ*, 114, 2157
- Haisch, K. E., Barsony, M., Greene, T. P., & Ressler, M. E. 2002, *ApJ*, 125, 2841
- Harker, D. E., Woodward, C. E., Wooden, D. H., Witteborn, F. C., & Meyer, A. W. 1999, *AJ*, 118, 1423
- Honda, M., et al. 2004, *ApJ*, 610, L49
- Huard, T. L., Weintraub, D. A., & Kastner, J. H. 1997, *MNRAS*, 290, 598
- Hurt, R. L. & Barsony, M. 1996, *ApJ*, 460, L45
- Ishii, M., Tamura, M., & Itoh, Y. 2004, *ApJ*, 612, 956
- Kaas, A. A. et al. 2004, *A&A*, 421, 623
- Kessler-Silacci, J. E., Hillenbrand, L. A., Blake, G. A., & Meyer, M. R. 2005, *ApJ*, 622, 404
- Knacke, R. F., Fajardo-Acosta, S. B., Telesco, C. M., Hackwell, J. A., Lynch, D. K., & Russell, R. W. 1993, *ApJ*, 418, 440
- Liu, M. C., et al. 1996, *ApJ*, 461, 334
- Mathis, J. S. 1990, *ARA&A*, 28, 37
- Meeus, G., Sterzik, M., Bouwman, J., & Natta, A. 2003, *A&A*, 409, L25
- Przygodda, F., van Boekel, R., Àbrahà, P., Melnikov, S. Y., Waters, L. B. F. M., & Leinert, Ch. 2003, *A&A*, 412, L43
- Rieke, G. H. & Lebofsky, M. J. 1985, *ApJ*, 288, 618
- Straizys, V., Černis, K., & Bartašiūtė, S. 1996, *Baltic Astronomy*, 5, 125
- Strom, S. E., Vrba, F. J., & Strom, K. E. 1976, *AJ*, 81, 638
- Telesco, C. M. & Knacke, R. F. 1991, *ApJ*, 372, L29
- Telesco, C. M., Piña, R. K., Hanna, K. T., Julian, J. A., Hon, D. B., & Kisko, T. M. 1998, *SPIE*, 3354, 534
- Testi, L. & Sargent, A. I. 1998, *ApJL*, 508, L91
- van Boekel, R., Waters, L. B. F. M., Dominik, C., Bouwman, J., de Koter, A., Dullemond, C. P., & Paresce, F. 2003, *A&A*, 400, L21
- Watson, D. M. et al. 2004, *ApJS*, 154, 391

TABLE 1
SUMMARY OF MID-INFRARED FLUX DENSITIES

λ_c (μm)	SVS20-S F_ν (Jy)	SVS20-N F_ν (Jy)	Comments	Reference
8.0	4.0 ± 0.1	2.6 ± 0.1	T-ReCS Spectroscopy	1
8.0		6.16 ± 0.14	ISOCAM CVF Binary Unresolved	2
10.4	5.4 ± 0.5	2.5 ± 0.2	TIMMI2 Photometry	1
10.78	4.36 ± 0.26	1.53 ± 0.09	MIRLIN Photometry	3
11.7	5.32 ± 0.27	2.80 ± 0.14	T-ReCS Photometry	1
11.9	4.7 ± 0.5	3.0 ± 0.3	TIMMI2 Photometry	1
12.0		8.5 ± 0.6	IRAS/HIRES Binary Unresolved	4
12.9	3.6 ± 0.4	3.2 ± 0.3	TIMMI2 Photometry	1

REFERENCES. — 1. This work, 2. Alexander et al. (2003), 3. Haisch et al. (2002), 4. Hurt & Barsony (1996)

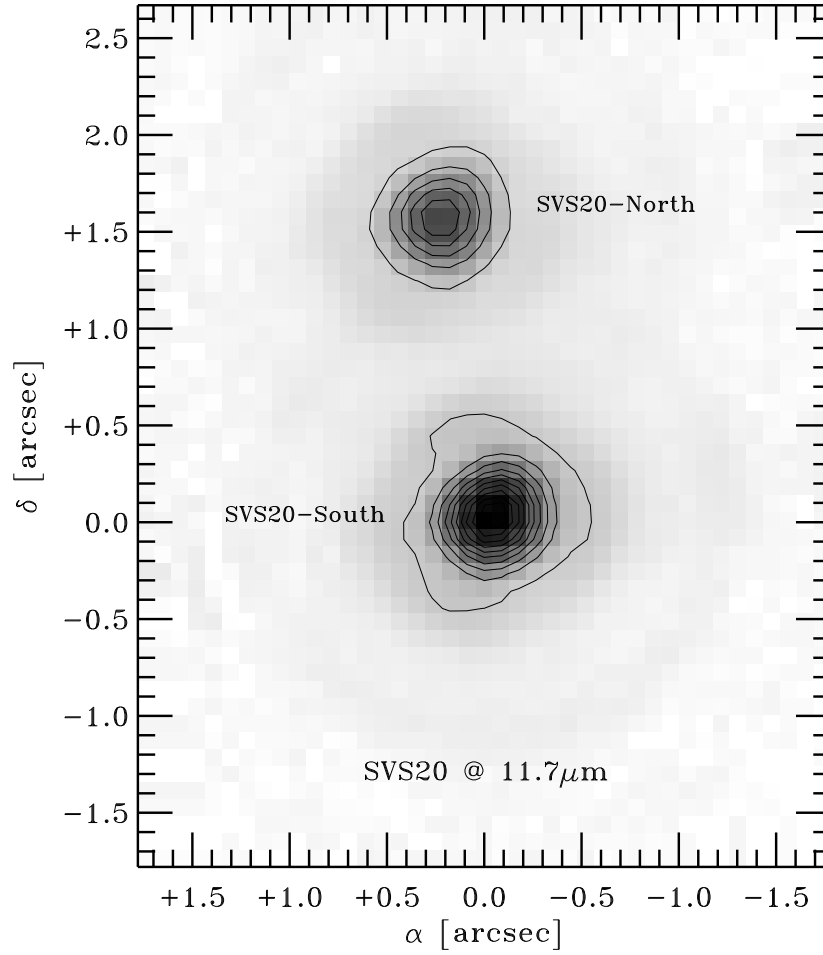


FIG. 1.— T-ReCS $11.7\mu\text{m}$ image of SVS20. The (0,0) point of the image is centered on SVS20-South at $\alpha = 18^{\text{h}}29^{\text{m}}58.7^{\text{s}}$, $\delta = 01^{\circ}14^{\circ}03.2^{\circ}$ ($J2000$). The greyscale has been stretched by a square-root to enhance the contrast. The contours are linear and start at 0.01 Jy pix^{-1} and are stepped by 0.02 Jy pix^{-1} .

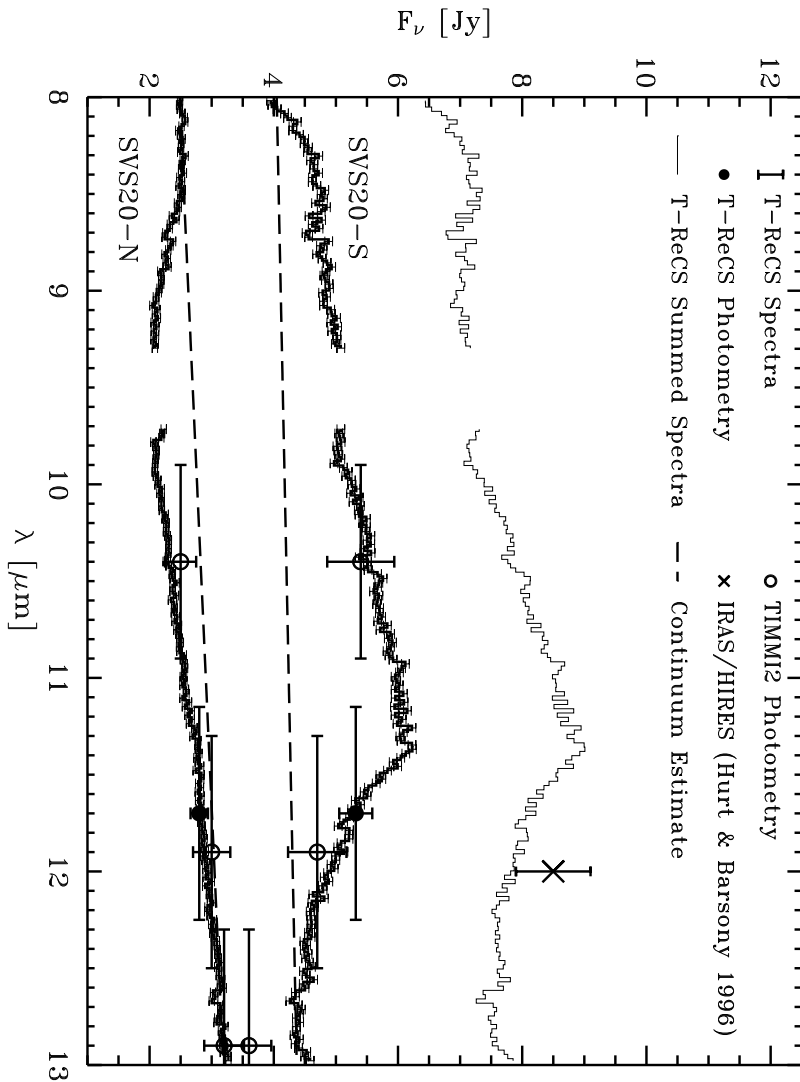


FIG. 2.— Mid-infrared spectra for SVS20-S and SVS20-N. The individual data points represent photometry presented in this work (T-ReCS & TIMMI2 photometry) and from the literature (IRAS). The summed spectrum is presented for ease of comparison to the unresolved IRAS photometry (Hurt & Barsony 1996) and the unresolved ISO spectra (not shown; Alexander et al. 2003). The data near telluric ozone ($9.3 < \lambda < 9.7 \mu\text{m}$) have been removed because of uncertain ozone subtraction. The abscissa error bars on the narrowband photometric points represent the widths of the narrowband filters. The continua estimates to the spectra are shown as the dashed lines.

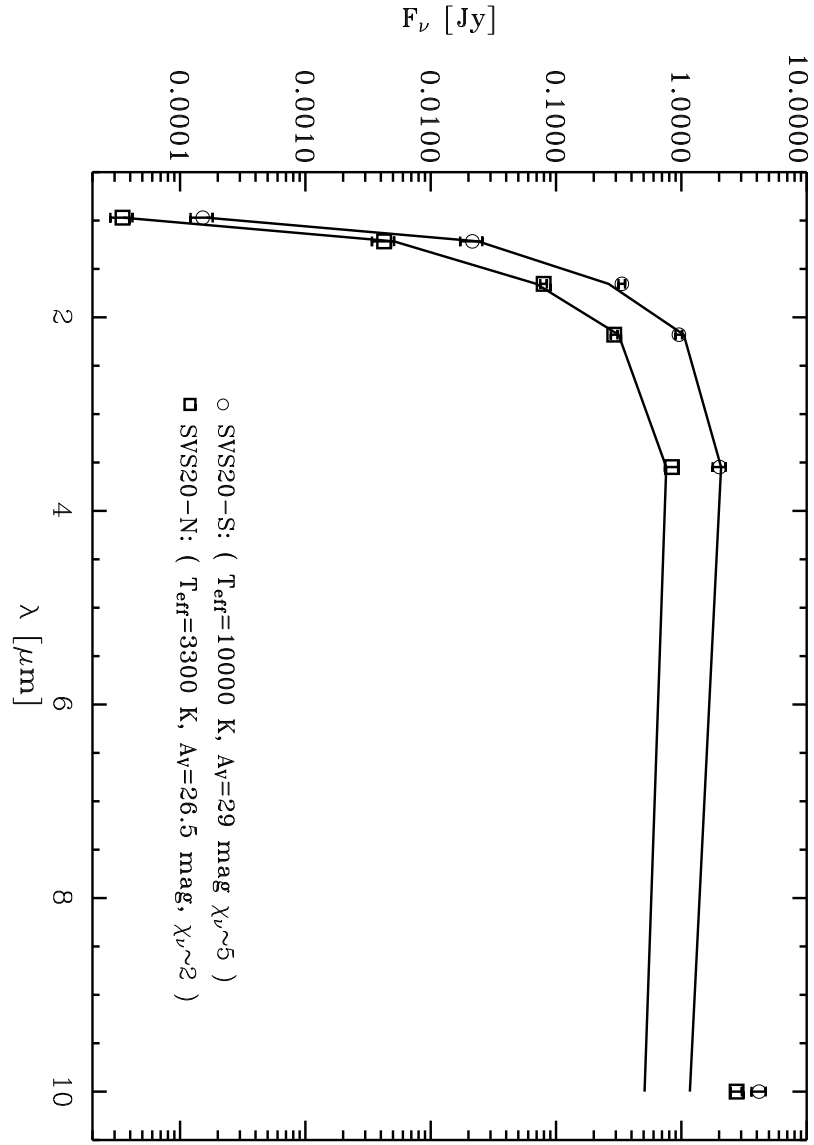


FIG. 3.— The spectral energy distributions for SVS20-S and SVS20-N. The models (solid lines) are extinguished single-temperature blackbody functions fit to the NIR data (Eiroa & Leinert 1987; Eiroa et al. 1987; Haisch et al. 2002). The 10 μm data, estimated from the *continuum* levels in Figure 2, are not included in the fitting.

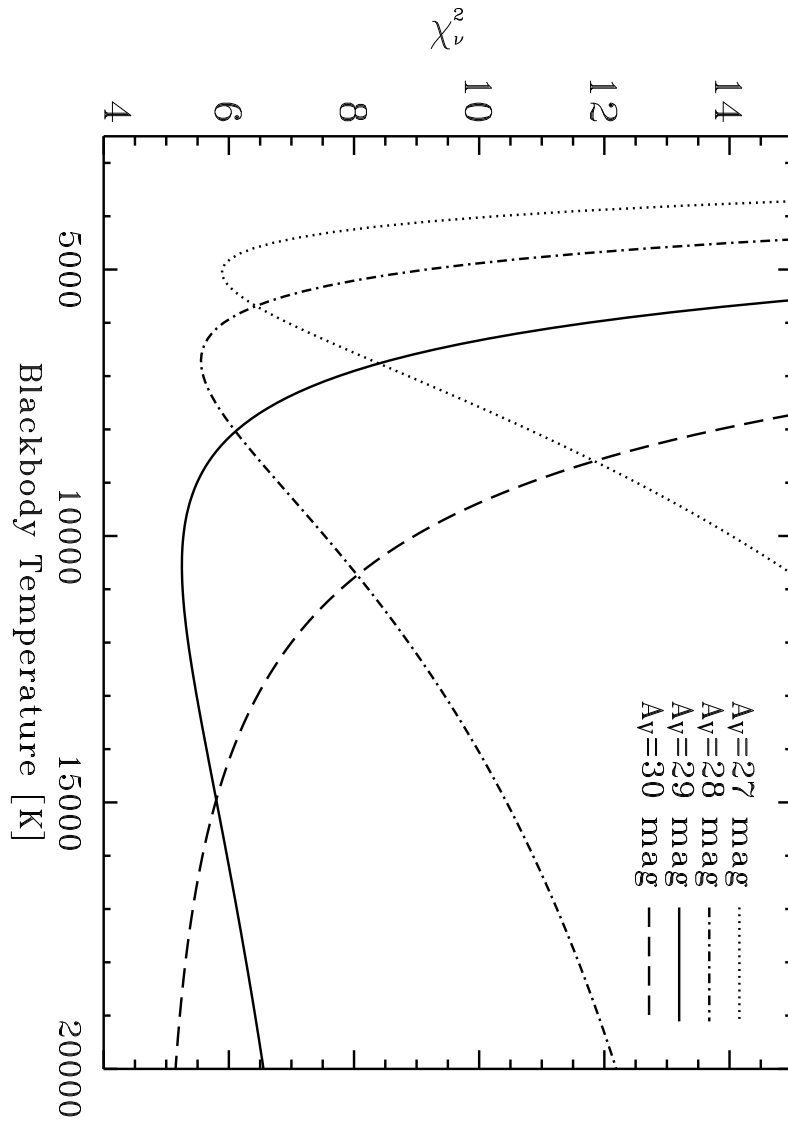


FIG. 4.— Plot of the reduced chi-square for the SED fits for SVS20-S as a function of temperature for four different visual extinction levels: $A_V = 27$ mag, 28 mag, 29 mag, and 30 mag.

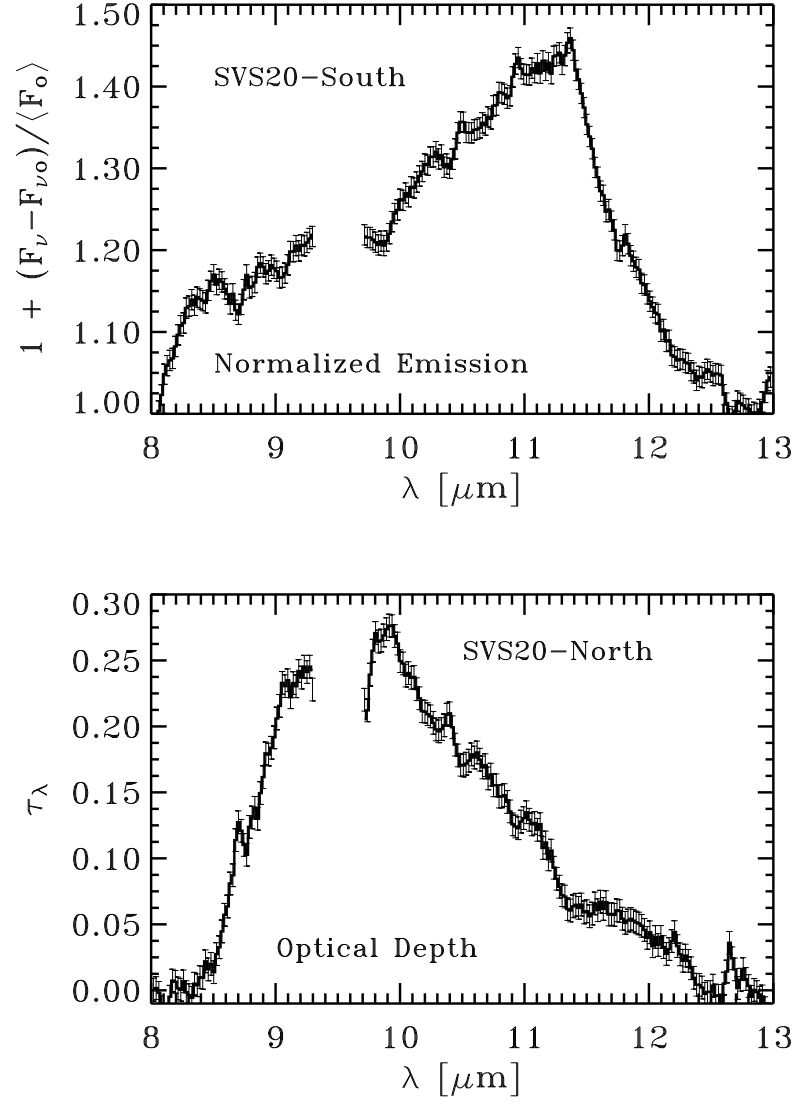


FIG. 5.— *Top*: Normalized emission of SVS20-South, median smoothed with a 3-pixel boxcar. *Bottom*: SVS20-North optical depth derived from the continuum-normalized spectrum, median smoothed with a 3-pixel boxcar.

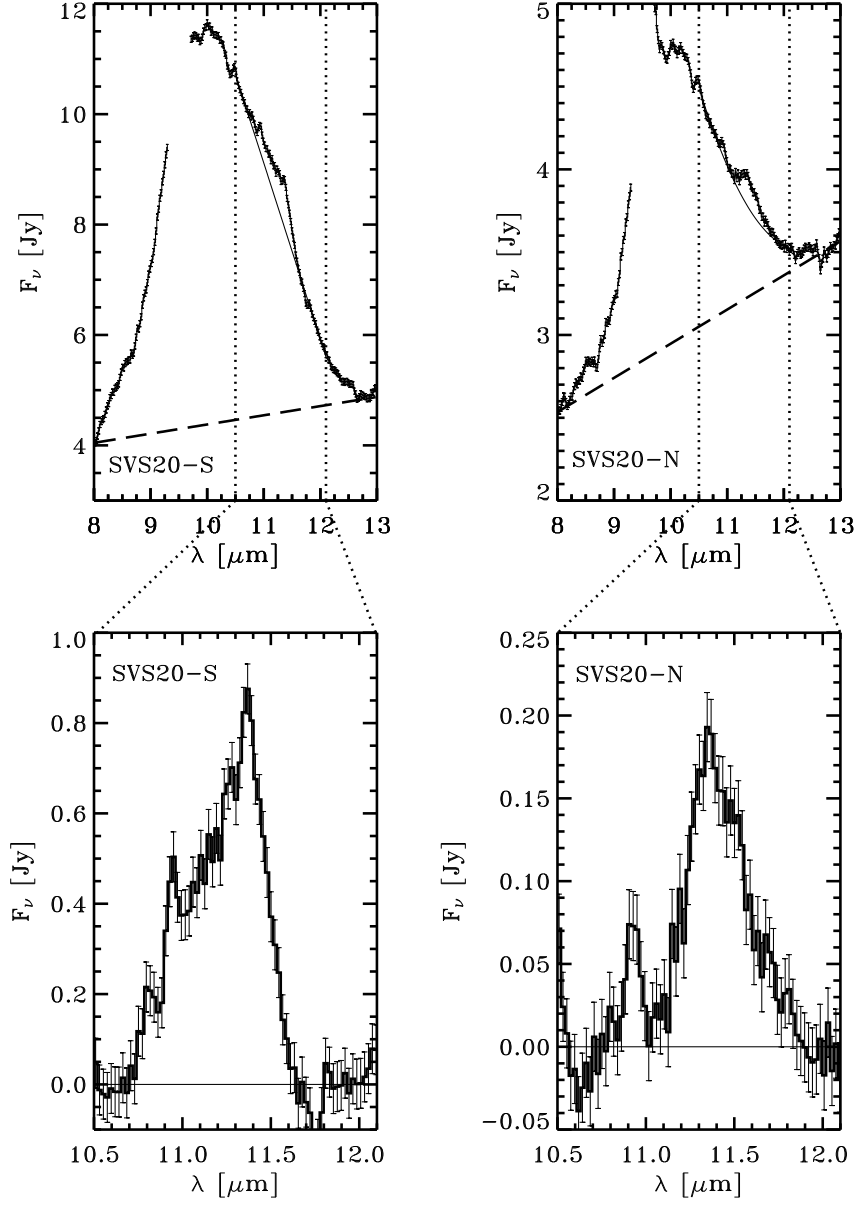


FIG. 6.— *Top*: Spectra for SVS20 after the removal of the envelope line-of-sight extinction model. The dashed line represents the continuum level for the overall emission. The dotted lines mark the wavelength range ($10.5 \leq \lambda \leq 12.1 \mu\text{m}$) fitted with a local continuum represented by the solid lines. Spectra have been median smoothed with a 3-pixel boxcar. *Bottom*: The $10.5 \leq \lambda \leq 12.1 \mu\text{m}$ spectra for SVS20-South and SVS20-North after the subtraction of the local continuum. Spectra have been median smoothed with a 3-pixel boxcar.